Lattice Model Simulation of Hydrogen Effect on Palladium Gold Alloys Used as Purification Metal Membranes

A Thesis
Presented to
The Academic Faculty

by

I. Namory Keita

In Partial Fulfillment
of the Requirements for the Degree
Master of Science in the
School of Chemical & Biomolecular Engineering

Georgia Institute of Technology
August 2012

Lattice Model Simulation of Hydrogen Effect on Palladium Gold Alloys Used as Purification Metal Membranes

Approved by:

Dr. David S. Sholl, Advisor
School of Chemical & Biomolecular Engineering
Georgia Institute of Technology

Dr. Michael A. Filler
School of Chemical & Biomolecular Engineering
Georgia Institute of Technology

Dr. Carsten Sievers
School of Chemical & Biomolecular Engineering
Georgia Institute of Technology

Date Approved: April 26, 2012

ACKNOWLEDGMENTS

I would like to thank my advisor Dr. David Sholl for giving me the tremendous opportunity to work on this project in his group. I learned how to extend my analytical thinking and problem solving in the research environment. Thank you for your teaching and guidance.

I would also like to thank the group members especially Nita Chandrasekhar, Emmanuel Haldoupis, and Sung Gu Kang who taught me crucial skills necessary for the completion of my work.

I would like to thank my family for their support. They instilled in me values of education, hard work and service.

Lastly, I would like to thank God who makes everything possible.

TABLE OF CONTENTS

LIST OF TABLES

LIST OF FIGURES

LIST OF SYMBOLS AND ABBREVIATIONS

CE = Cluster Expansion

SRO = Short Range Order

NVT-MC = constant Number of atoms, constant Volume and Temperature - Monte Carlo

LOO = Leave One Out

FCC = Face Centered Cubic

DFT = Density Functional Theory

at.% = Atomic percent

NEB = Nudged Elastic Band

Atm = Atmospheric pressure

SUMMARY

Hydrogen fuel is seen as energy of the future. Hydrogen molecules (H_2) are mostly used in the petrochemical industry and ammonia production. Hydrogen molecules are produced in large majority by steam reforming of hydrocarbons (methane). However, the purification of hydrogen is still a major factor in the cost of producing hydrogen. The range of membranes is large with advantages and drawbacks of each type of membrane. Among those membranes, metal alloy membranes are widely used because of their selectivity, durability, and resistance to poisoning. In the past, it was assumed an alloy once formed would remain in its initial structure while hydrogen gas was permeating through. It has been shown experimentally that the presence of hydrogen in palladium gold metal alloys will change the structure of the alloy from a disordered to an ordered phase. Hydrogen isotherms at different temperatures were used to demonstrate the change in structure. This structural change resulted in an increase in solubility of hydrogen in the membrane. In this work, using NVT-Monte Carlo we calculated the effect of hydrogen on the structure and on the solubility of $Pd_{96}Au_4$ and $Pd_{85}Au_{15}$ alloys. The palladium gold alloy was used because it demonstrated high resistance to sulfur poisoning and similar or higher permeability seen in to pure Pd. The methods used do not require any experimental input except for the structure of the bulk crystal. The interstitial binding energies were calculated using a Cluster Expansion model derived previously by Semidey and Kang from plane wave Density Functional Theory. The metal atoms enthalpies of formation were calculated from a truncated version of the Cluster Expansion derived by Sluiter for fcc metal structures. We conclude that hydrogen presence in the metal membrane will change the membrane from a disordered to a Short Range Ordered structure.

CHAPTER 1: INTRODUCTION

The hydrogen economy is a potential long term solution to the growing energy crisis [1]. However, economic barriers exist such as the cost of fuel cells and the cost of hydrogen production which must be reduced by factors of 10 and 4 respectively for hydrogen to be economically feasible [1]. There are several major processes to purify hydrogen including pressure swing adsorption (PSA), cryogenic distillation, and membrane separation. Among these methods, membrane separation has great potential for being an efficient and cost effective process [1]. Currently, 90% of hydrogen is generated from fossil fuel via steam reforming of hydrocarbons, while a smaller fraction is from water hydrolysis. Steam reforming of methane consists of mixing methane with steam at high temperature (~820 °C) to produce hydrogen, water, carbon monoxide and carbon dioxide. At 350 °C a typical product stream contains 73.9% H_2, 17.7% CO_2, 6.9% CH_4, 1 % CO and 0.5% H_2O [1]. It is desirable to purify this stream to produce pure hydrogen (99.99%).

The US Department of Energy (DOE) has defined a number of objectives for membrane-based purification of hydrogen. These include an aim to reduce membrane cost to under $\$100/ft^2$, to increase the hydrogen flux at temperatures between 250 and 500°C, to improve durability of membranes to more than 5 years, and to achieve >90% recovery with high purity (99.99% pure H_2) [1]. There is a wide range of materials available for hydrogen separation with advantages and limitations in chemical, thermal and mechanical stabilities (metals, silica, zeolite, carbon nanotubes, polymer, etc.) [1]. The key characteristics of membranes for this application are the membrane permeance (flux) and selectivity. The flux is the amount of gas that permeates

through the membrane per time and unit surface area [1]. The selectivity is the capability of a membrane to separate different gases [1].

Throughout this thesis, we consider hydrogen permeation through dense metal membranes. The driving force for gas diffusion through dense membranes is the hydrogen chemical potential (concentration gradient) which is represented in Ficks' first law [1.1]:

$$J_{H_2} = -D_{H_2} \nabla C_{(x,y,z)} \qquad \nabla C_{(x,y,z)} = i\frac{\partial C}{\partial x} + j\frac{\partial C}{\partial y} + k\frac{\partial C}{\partial z} \tag{1.1}$$

where D_{H2} is the diffusion coefficient and $\nabla C(x,y,z)$ is the three-dimensional concentration in Cartesian coordinates [1]. For a membrane, we will only consider the concentration gradient in one dimension [1]. In many materials, the relationship between concentration in a membrane material and the external pressure is given by Henry's law [1]:

$$S_H = \frac{C_{gas}}{P_{gas}} \tag{1.2}$$

where S_H is a constant relating the vapor pressure of a non-dissociative gas to its dilute concentration in a liquid or solid, and C_{gas} and P_{gas} are the concentration in the membrane and the pressure of the gas, respectively [1]. In metal membranes, however, molecular hydrogen undergoes dissociation before diffusing through a membrane. In this case, the appropriate connection between the external pressure and the concentration of atomic H in the membrane is Sieverts' law [1]:

$$S_H = \frac{C_{gas}}{P_{gas}^{1/2}} \tag{1.3}$$

This expression is only valid if the concentration of atomic H is low [1]. By combining equation (1.3) and (1.1), the net flux of hydrogen through a membrane can be expressed as:

$$J_{H_2} = \frac{-D_{H_2}\partial C}{\partial L} = \frac{-D_{H_2}S_{H_2}\partial P_{H_2}^{1/2}}{\partial L} \cong \frac{-D_{H_2}S_{H_2}\Delta P_{H_2}^{1/2}}{\Delta L} = \frac{-D_{H_2}S_{H_2}(P_{H_2,L}^{1/2} - P_{H_2,0}^{1/2})}{2*L} \quad (1.4)$$

where J_{H2} is the hydrogen flux, L is the membrane thickness, and $P_{H2,0}$ and $P_{H2,L}$ are the hydrogen pressures at the feed and product side of membrane [1]. This expression is valid when the diffusion of H in the bulk of the membrane is the rate limiting step. The other case of surface rate limiting step for ultra-thin alloy films membrane have been investigated by Chen and Sholl [21]. The product of D_{H2} and S_{H2} is called the hydrogen permeability [1]:

$$k = \frac{S_{H_2} * D_{H_2}}{2} \quad (1.5)$$

Molecular hydrogen is dissociated to give atomic H by a catalytic surface on the feed stream of the membrane and after hopping through interstitial sites recombines on the product side [1]. This mechanism can be seen in Figure 1.

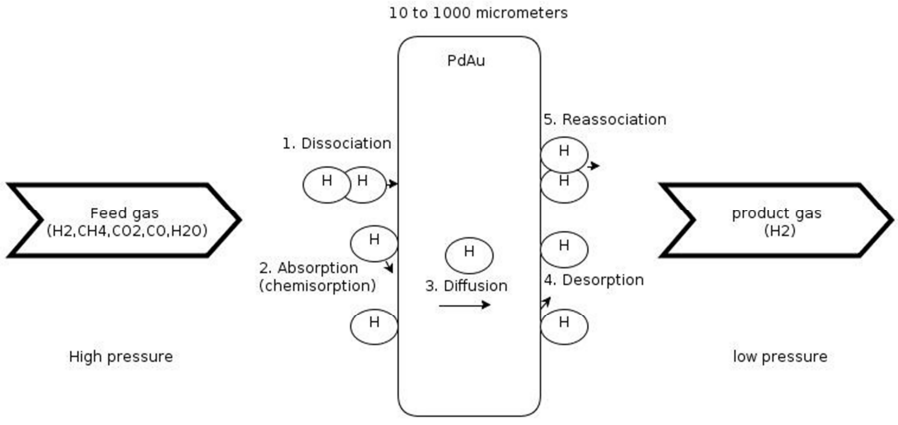

Figure 1. Hydrogen diffusion mechanism in dense metal. Steps: 1.dissociation, 2. adsorption (chemisorption), 3. Diffusion, 4. Desorption, 5. Reassociation. Redrawn from [1].

Metal membranes are a useful approach for hydrogen purification because of their infinite selectivity [1]. The mechanism of this selectivity follows from Figure 1, since the ability of atoms other than H to move through a dense metal by interstitial diffusion is extremely limited due to the small interstitial site size. Metals can have different structures such as pure metals, crystalline alloys and amorphous alloys [2]. Each of these structures has been considered as membranes for hydrogen purification. Below, some key features of these types of metal membranes are described.

Hydrogen permeability in pure metals is a function of the crystal lattice structure, chemical reactivity and lattice defects [2]. Pure metals have drawbacks such as formation of stable hydrides which causes hydrogen embrittlement (leading to significant membrane degradation), low catalysis capabilities (dissociation and reassociation of hydrogen molecules) leading to slow hydrogen flux, and contamination of surface by oxides impeding the absorption of hydrogen [2]. Palladium is the preferred pure metal because it naturally catalyzes hydrogen surface dissociation [1]. However, sulfur contamination causes an irreversible permeance loss and failure of Pd membranes due to pinholes and bulk sulfidation [3]. In addition, below 300 °C palladium forms a hydride that degrades the membrane via hydrogen embrittlement because of the difference in the lattice constants between the metal and the hydride [1]. Kamakoti P. and Sholl D. developed an Ab initio lattice gas model to calculate the binding energies of hydrogen in pure Pd in order to compute the diffusivity of H [15]. The model described with semi-quantitative accuracy the diffusion of H compared to experimental results. The diffusivity of H was over predicted even though the trend of the change of the diffusivity as a function of temperature was captured [15].

The second category of metal membranes is crystalline alloys. The objective of alloying is to improve physical, chemical, and poisoning resistance properties. Alloying palladium with other metals such as Ag, Cu, or Au can reduce the formation of hydrides and surface contamination [1]. For example, when $Pd_{92}Au_8$ was exposed to 54.8 ppm H_2S/H_2 it showed resistance to bulk sulfidation at temperatures ranging from 350-500 °C without structural modification [3]. Site blocking by dissociative adsorption of H_2S on this material reduced membrane permeance, but was reversible [3]. In another alloy ($Pd_{70}Cu_{30}$) the permeability remained constant for 1000 micrometer foils between 623-1173 K when exposed to 1000 ppm H_2S for more than 175 hours [4, Fig.4]. For thinner PdCu membranes ($Pd_{40}Cu_{60}$, 10 micrometers) the permeability of H_2 decreased by half when exposed to 630 ppm H_2S [3]. However, the permeability reverses to pre-contamination levels when exposed to pure H_2 [5]. Recently a lattice model was developed by Kamakoti and Sholl which calculated the theoretical diffusivity of $Pd_{43}Cu_{57}$ at 700 K to be 1.42×10^{-9} m^2/s [15]. This result over predicted the experimental value of 6.14×10^{-10} m^2/s [15]. However, the model captured the change in diffusivity with respect to the alloy composition and temperature [15]. Later Semidey and Sholl developed another lattice model involving more body interactions and calculated solubility, diffusivity and permeability [13]. The model predicted the permeability of H in $Pd_{96}Ag_4$ at 773 K to be 1.5 times larger than pre Pd [13]. This result is in good agreement with experimental results predicting the permeability of $Pd_{90}Ag_{10}$ at 773 K to be around 1.5 times larger than the permeability of pure Pd [13].

The third class of metal membranes is based on amorphous metals. Amorphous metals can have better mechanical and structural properties than crystalline metals. Amorphous metals are less prone to defects [1]. A limitation of amorphous membrane is their crystallization at T >

500 ° C [1]. Hence, the amorphous membranes are limited to low operating temperatures and as a result exhibit low fluxes [1]. Shiqiang and Sholl predicted using computational calculations that two amorphous ($Zr_{54}Cu_{46}$ and $Zr_{30}Cu_{60}Ti_{10}$) membranes had permeabilities (fluxes) similar to that of pure Pd above 600 K [16]. Another amorphous ($Zr_{30}(Ni_{0.6}Nb_{0.4})_{70}$) demonstrated permeabilities in the same range seen for crystalline Pd [17].

Existing descriptions of metal membranes for hydrogen purification typically assume that the state of the metal membrane with and without the presence of hydrogen is the same. There is experimental evidence, however, that this assumption is not always reasonable. Examples are known where high temperature and hydrogen pressure can cause a disordered face centered cubic (fcc) crystalline alloy to form a hydrogen-stabilized ordered phase [6]. This phenomenon is known as Hydrogen Heat Treatment (HHT) [6]. HHT is a phenomenon which is believed to have a kinetic role in enhancing metal atom rearrangement from disordered to ordering and an important role in shifting equilibrium from a disordered to hydrogen stable ordered alloy [6]. In the absence of hydrogen at the same operating conditions the alloy returns to its disordered phase if equilibrium is reached [6]. There is some evidence that HHT enhances metal atom diffusion due to an increase in vacancy concentration in the bulk phase [8]. Flanagan et al. observed that when Pd_3Mn in the disordered state was exposed to high hydrogen pressures (1 to 5 Mpa) it formed an ordered state (L_{12}) at a temperature of 423 K [7]. Ordering did not occur at the same conditions in the absence of hydrogen [7]. The ordering was not complete at low temperatures but complete ordering occurred at 5 Mpa and 723 K [7]. In addition, $Pd_{60}Cu_{40}$ and $Pd_{50}Ag_{50}$ changed from a disordered to an ordered structure at high hydrogen pressures and temperatures above 493 K. However, at high temperature and pressure Pd-Rh, Pd-Ni and Pd-Pt segregated due to a ternary equilibrium (Pd+M+H) [6]. Pd-Au alloy is a promising alloy because of the high

permeability and resistance to sulfur contamination. Palladium gold alloys with gold compositions ranging between 10 and 25 at.% showed experimentally 2 to 5 fold higher permeability compared to pure palladium [9] and better resistance to sulfur poisoning [34].

The PdAu alloys form disordered face centered cubic (fcc) structures at all temperatures except for some compositions. Experimental phase diagrams are scarce for PdAu. Okamoto and Massalski reported a region between 12-30 at.% Au at temperatures ranging from 973 to 1143K where the L_{12} structure $AuPd_3$ is observed. The critical temperature for the phase change (order to disorder) was measured to be 1053 K [18]. Another region reported by Okamoto is at 68-88 at.% Au for temperatures of 873-1123 K where the observed structure is Au_3Pd. Here the critical temperature was 1133 K [19]. The last region is for AuPd for 43-57 at.% Au for temperatures up to 373K [12]. The critical temperature was 373 K [20].

Sluiter et al. calculated using Ab initio calculations the enthalpies of mixing of the AuPd alloy in order to observe the phase diagram [14]. The authors did not agree with all the temperatures for order-disordered phase changes found experimentally by Okamoto et al. [12]. The authors claim that because there are no other phase diagrams with the high experimental critical temperatures for $AuPd_3$ and Au_3Pd the results (400 and 500 K) that they find seems more accurate [14]. However, the authors agreed with the reported critical temperature for equiatomic PdAu for which they found 423 K [14]. Another ordered phase (long period superlattices) might also be present even though it could not be captured with the current calculations [14].

In this paper we use theoretical methods to study the change in the structure of disordered PdAu alloys due to hydrogen thermodynamic phenomena and the effect of these changes on solubility of hydrogen through PdAu membranes. To achieve this goal, we combine two

problems that have been examined previously using quantum chemistry-based methods. The solubility and diffusion of interstitial H in PdAu alloys has been examined previously by Semidey-Flecha et al. [13], and we use the models developed in that work to describe H interactions with the various local configurations available in PdAu alloys. A detailed model for the energy associated with rearranging Pd and Au atoms on the fcc structure defined by a PdAu alloy has been reported by Sluiter et al. [14]. We use this description to account for metal-metal interactions in PdAu alloys.

The simulation method that we use is the Monte Carlo method which is a statistical computation that uses consecutive random sampling to approximate a physical system or compute a mathematical problem [38]. The Monte Carlo simulation is particularly suited for systems with multiple degrees of freedom such as disordered materials. The method was developed by scientists Ulam, Neumann and Metropolis while working at Los Alamos Laboratory in the 1940's [38]. Monte Carlo calculates equilibrium averages on system ensembles. In this work we will use the Metropolis Method which uses a sequence of random samples from a probability distribution (Boltzmann distribution) [39].

CHAPTER 2: COMPUTATIONAL METHODS

In order to calculate the physical properties of H in solid alloys the binding energies of H in interstitial sites have to be calculated [11]. Plane wave Density Functional Theory (DFT) is an accurate quantum mechanical method used to compute the binding energies and vibrational frequencies of atomic hydrogen in solid alloys [11, 31]. DFT is a first principles theory of electronic ground-state structure based on the electron density distribution [11, 31]. DFT can calculate the ground state electron density and total energy of a system with nuclei and electrons. The calculations can be performed on any element in the periodic table including materials with metallic, covalent and ionic bonds [11, 31]. Isolated, surfaces, and bulk solids can all be evaluated with DFT [11, 31]. Calculations for bulk solids are performed using a central super cell which is repeated with periodic boundaries in three dimensional spaces in order to mimic the infinitely large solid [11, 31]. Numerous calculations have proven that DFT is quantitatively accurate for the calculations of the potential energy and vibrational frequencies of hydrogen atoms absorbed in metals and metal surfaces [22-28].

The DFT calculations used to parameterize the model to calculate the interstitial binding site's energies were completed using the Vienna *Ab initio* Simulation Package (VASP) [32]. The ultra-soft pseudo potentials introduced by Vanderbilt were used to describe the interactions between the ions and the electrons [32]. The generalized gradient approximation (GGA) was implemented to describe the electron exchange correlation effects using the Perdew-Wang 91 functional [33]. A plane wave expansion with a cutoff of 233.7 eV was used. The total energy calculations used the residual minimization method for electron relaxation, accelerated using the Methfessel-Paxton Fermi-level smearing with a width of 0.2 eV. Geometry relaxations were done with a conjugate gradient algorithm until the forces on all atoms were less than 0.3 eV/ Å.

A Γ-centered grid of 4x4x4 *k*-points was used to sample the reciprocal space for all calculations with bulk materials. These parameters were previously used for metal alloys and proved to optimal for convergence and accuracy [11]. Using these methods, the lattice constant for pure Pd was calculated to be 3.960 Å which is around 2% larger than the experimental value of 3.889 Å [11]. In order to calculate the binding energy of H in an interstitial site the following equation is used [11]:

$$E_b = E_{H+M} - E_M - \frac{1}{2}E_{H_2} \tag{2.1}$$

where E_{H+M} is the energy of the metal with hydrogen, E_M is the energy of the metal without hydrogen and E_{H2} is the energy of H_2 gas [11]. There are two types of interstitial sites or binding sites in fcc metals. The hydrogen can bind in the sixfold octahedral (O) and the fourfold tetrahedral (T) sites. The calculated pure Pd binding energy in the O site is $E_{b,O}$=-0.14 eV and for the T site $E_{b,T}$=-0.09 eV [11]. At zero temperature, H has a minimum energy that is called the zero point energy (ZPE) correction which can be calculated using:

$$E_H{}^{ZP} = h\sum_{i=1}^{3}\frac{\upsilon_i^H}{2} \tag{2.2}$$

where h is Planck's constant and ν_i are the vibrational frequencies of H [11]. These frequencies can be calculated within the harmonic approximation by assuming that the vibrational modes of interstitial hydrogen are decoupled from lattice phonons [11]. The H in an octahedral site of pure pd $E_H{}^{ZP}$ was equal to 0.10 eV and $E_{H2}{}^{ZP}$ was equal to 0.270 eV which agree well with experimental results [11]. To account for zero point energies, the classical binding energy for an interstitial site must be corrected to [11] :

$$E_b^{ZP} = E_b - E_H^{ZP} - \frac{1}{2} E_{H_2}^{ZP} \tag{2.3}$$

A substitutionally disordered alloy has many sites that differ in their local coordination, and calculation of all individual sites would be computationally expensive [13]. A useful approach to this issue is to develop a lattice model (Cluster Expansion) parameterized with DFT calculations in order to calculate the binding energy of H in different interstitial sites (octahedral and tetrahedral) [13]. A cluster expansion (CE) calculates the interactions between clusters of some particle (1, 2, 3 … body interactions) [13]. The total energy of a configuration can be represented as a linear combination of an infinite energy series [13]. An example of a cluster expansion up to 3 body interactions at the Next Nearest Neighbor distance to calculate H binding energies is

$$E_b = E_o + \sum_i J_i^{(1)} \sigma_i^{(1)} + \sum_i J_i^{(2)} \sigma_i^{(2)} + \sum_i J_i^{(3)} \sigma_i^{(3)} + \ldots \tag{2.4}$$

Here, J_i are the interaction energies, which are fitted in a least-squares sense to DFT calculations for different sites [13] and σ_i is a configurational model using spin variables. For example, if using the Ising spin model with S_{Pd}=1, S_{Au}= -1, then the configuration of the atoms in the nearest neighbor shell is:

$$\sigma_{NN}^{(1)} = \sum S_i \tag{2.5}$$

where i is either Pd or Au [13].

It is important to note that this CE was developed based on DFT calculations using hundreds of distinct configurations and statistical methods were used to ensure that the parameters used in the final CE are significant. Specifically, the leave one out (LOO) method

was used [13]. The LOO compares models with different number of parameters in order to calculate the most accurate model. A LOO analysis consist of performing a least squares minimization of the model being considered X independent times where in each case, one data point from the complete set of X values is left out. The LOO error is found from these calculations:

$$R^2_{LOO} = \frac{1}{X}\sum_{k=1}^{X}(E_{\text{predicted,k}} - E_{\text{k}})^2 \qquad (2.6)$$

where E_k is the k-th data point and $E_{predicted,k}$ is the value for this point predicted by the model fitted to all the data except the k-th data point. The model with the lowest R^2 gives the best model. The binding site calculations for $Pd_{96}Au_4$ alloy done with the Cluster Expansion agreed well with the DFT calculated energies. In addition, the plot of the cumulative probability proved that the CE was able to capture all the lowest binding energies in the $Pd_{96}Au_4$ alloy [13].

A CE for H in $Pd_{96}Au_4$ was developed earlier by Semidey-Flecha and Sholl [13]. For this PdAu alloy the infinite series was truncated to 20 parameters to describe O sites. This approach includes configurations with up to 4-body interactions [13]. Similarly, 30 parameters were used for the T sites with up to 3 body interactions [13]. In order for H to diffuse, it has to hop between O and T sites through Transition States (TS) [13]. The transition state model was parameterized as a combination of the O and T parameters [13]. Hence, there are 50 TS parameters [13]. All the parameters were also calculated for the zero point energy of the interstitial sites. The values for O, T and TS site parameters for $Pd_{96}Au_4$ were calculated and described by Semidey-Flecha and Sholl [Appendix A, 13]. A limitation of the CE developed by Semidey-Flecha et al. is that it only applies to a specific PdAu alloy. To allow examination of another alloy composition, a new

CE for interstitial H in $Pd_{85}Au_{15}$ was developed in this work. More details on the derivation and performance of this CE are presented in the results section.

Once the binding energies and vibrational frequencies of individual interstitial sites are defined, the solubility, diffusivity and permeability of H in a material can be calculated.

Hydrogen dissolves in metal alloys via dissociative absorption of molecular H_2 as shown here in Eq.(2.7):

$$H_2(g) \leftrightarrow 2H(a) \tag{2.7}$$

Eq.(2.7) corresponds to a situation where H atoms dissolved in a metal/alloy are in equilibrium with gaseous H_2 in the neighboring gas phase having a partial pressure P. We define the concentration of H atoms, θ_H, as the ratio of the number of H atoms dissolved to the total number of metal atoms in the system. The solubility or loading of dilute hydrogen follows Sieverts' law:

$$\theta_H = K_s\sqrt{P_{H2}} \tag{2.8}$$

where θ_H is the ratio of number of H atoms dissolved to the total number of metal atoms in the system, K_s is the Sieverts' constant, which is the relationship between the interstitial concentration of atomic H and the gas phase H_2 pressure, P_{H2} (atm) [13]. Eq.(2.8) is only valid for dilute concentrations of interstitial H solutions. The Sieverts' Law is accurate for hydrogen dissolving in Pd at temperature ranges 873-143 K and pressures up to 1 atm [13]. These conditions lead to the α-PdH phase, where the low concentration of H atoms in the Pd interstitial sites is disordered. As T is lowered below 873 K or the pressure is raised, deviations are

observed because of the ordered β-PdH phase. In the calculations the solubility is always smaller than 0.1, where Sievert's Law still applies to the system. The chemical potential for H atoms, $\mu_{H,}$ is equated to the H_2 chemical potential, μ_{H2}, as shown below:

$$\frac{1}{2}\mu_{H_2(g)} = \mu_{H(a)} \tag{2.9}$$

Using the partition function for diatomic ideal gas in the Helmholtz free energy, we can express the Sievert's constant for an individual site, $K_{s,ind}$ as:

$$K_{s,ind} = \exp(-\beta\left[-\frac{D_E}{2}+\frac{h\nu_{H_2}}{4}-E_{b,H}-\frac{3}{2}h\nu_H\right])\frac{1}{\sqrt{\alpha}}\frac{\sqrt{1-\exp(\frac{-\beta h\nu_{H_2}}{2})}}{\prod_{i=1}^{3}\left(1-\exp(\beta h\nu_{H,i})\right)^3} \tag{2.10}$$

where

$$\alpha = \left(\frac{2\pi m k_b T}{h^2}\right)^{\frac{3}{2}}\frac{8\pi^2 I(k_B T)^2}{\sigma h^2}$$

Eq.(1.15) gives the H solubility at one interstitial site with binding energy E_b and vibrational frequency ν_H. The subscript i in Eq.(1.15) indicates that there are three vibrational frequencies for the interstitial H. The net Sieverts' constant for the material $K_{s,}$ is obtained by summing $K_{s,i}$ over all possible individual sites:

$$K_s = \sum K_{s,i} \tag{2.11}$$

The calculations of the binding energy E_b vibrational frequency ν_H were discussed previously.

Hydrogen diffusion in a fcc solid at high temperature is through hops between the 6-fold octahedral (O) and 4-fold tetrahedral (T) binding sites [13]. There is a transition state (TS)

between the O and T site where hydrogen has to go through for the hop. The TS location was calculated using the Nudged Elastic Band (NEB) method.

The rate of hopping for O-T jumps can be calculated using quantum corrected harmonic transition state theory:

$$k_{OT} = \frac{\prod_{i=1}^{3} f\left(\frac{h\upsilon_i^{o}}{2k_B T}\right)\prod_{i=1}^{3}\upsilon_i^{o}}{\prod_{i=1}^{2} f\left(\frac{h\upsilon_i^{TS}}{2k_B T}\right)\prod_{i=1}^{2}\upsilon_i^{TS}} e^{\frac{-E_a}{k_B T}} \qquad (2.12)$$

where f(x)=sinh (x) /x , and υ_i^{o} are the real vibrational frequencies of the binding site or TS, and E_a is the classical activation energy for a hop . The same equation can be used to calculate the rate of hopping for T-O jumps. This equation includes contributions from the multiple vibrational energy levels available to the interstitial H at a defined temperature. This equation can be modified to include tunneling between sites. However, it is assumed that the tunneling effect is negligible at the temperatures used (400-1200K) [13].

Once, the local hopping rates are calculated a Kinetic Monte Carlo simulation is used to simulate the hopping dynamics within a lattice model to get the net diffusivity of interstitial H in alloys [13]. The KMC algorithm models stochastic systems defined by a succession of events with known rates [13]. The energy minima map of the system is needed for KMC to accept or reject moves with appropriate probabilities [13]. After a large number of hops, the mean square displacement of each H is calculated. Then, with the correction for passage across periodic boundaries, the self-diffusivity, D_s (m^2/s), is computed using Einstein expression which relates the diffusivity to the mean square displacement:

$$D_s = \lim_{t->\infty}\left[\frac{1}{6Nt}\sum_{t=1}^{N}\left\{|\, R_i(t) - R_i(0)\,|^2\right\}\right] \tag{2.13}$$

where $R_i(t)$ is the position of an atom at time t, the angular bracket is the average over all atoms, N is the number of atoms [13]. Once the solubility and diffusivity have been calculated, the permeability can be calculated as presented in the introduction using equation (5).

An important goal of this work is to explore the relationship between the presence of interstitial H in PdAu alloys and ordering in these alloys. Once the crystal structure of alloy is known, the alloy can be ordered, disordered, or show short range order (SRO) among the lattice sites defined by the crystal structure [11]. Ordered structures have a repeating structure with the crystal lattice. For example, Pd_3Au which has the L_{12} structure has Pd atoms at the faces and Au at the corners of the fcc cube [11]. Disordered alloys, also known as substitutionally disordered materials, have the species making up the material distributed randomly among the lattice sites. Structures with SRO lie between these two extremes [11]. Cowley developed a SRO parameter α_j:

$$\alpha_j = 1 - \frac{p_j^{Au(Pd)}}{X_{Pd}} \tag{2.14}$$

where $p_j^{Au(Pd)}$ is the conditional probability that given Au atom at the origin, there is a Pd atom at the j^{th} neighbor distance. The sign of α_j shows whether the atoms favor ordering ($\alpha_j < 0$) or clustering ($\alpha_j > 0$) [29]. The SRO parameters range between -1 and 1. For a completely random structure, α_j is zero [29].

In a number of the calculations below, we studied interstitial H in PdAu alloys with specified SRO parameters. The calculations were only done on the chemical ordering with respect to the nearest neighbor shell (j=1, α_1). We used the Reverse Monte Carlo method to generate a structure with a specific α_1 and calculated the solubility of the structure [11]. The initial step in this process is to create a random structure (SRO parameter α_1 ~0) with Pd and Au atoms distributed randomly on an fcc lattice [11]. Next, an atom is randomly selected and swapped with another atom [11]. This move is accepted if the new SRO parameter is closer to the target SRO parameter with probability of unity and a fraction of the remaining moves are accepted with probability $\exp(-\beta \mid \alpha_1 - \alpha_{target} \mid)$, where β is an adjustable parameter ranging from 0.005 to 0.009 for different α_{target} [11]. This method has been used previously to reproduce structures with specified SRO parameters [11].

To explore the interplay between interstitial H and the ordering of PdAu alloys, it is necessary to have a quantitative model for the relative energy of different ordering states of metal atoms in an alloy. The PdAu alloy can have different configurations at different compositions; hence we will introduce another lattice model that was developed by Sluiter to calculate the enthalpy of formation of ground state structures for PdAu [30]. In Sluiter's work, a Cluster Expansion (CE) was developed based on DFT calculations to calculate the enthalpy of formation of PdAu alloy at different compositions [30]. The enthalpy is expanded in terms of composition-independent effective cluster interactions:

$$\Delta H_f{}^{\alpha} = \sum_i V_i \xi_i{}^{\alpha} \tag{2.15}$$

where V_i are the effective cluster interactions (ECI) found from DFT calculations of several structures [30]. ξ_i^{α} is the correlation function found from counting Pd clusters [30]. The structure inversion method was used to truncate the infinite series [30]. The final CE included 23 clusters [30]. These clusters include one point, nearest neighbor pairs, next nearest neighbor pairs, two nearest neighbors and one next nearest neighbor triplets, etc [30]. The calculated enthalpies of formation agreed well with DFT values [30]. For example, the enthalpy of formation of AuPd in the L_{10} ordered structure was calculated to be -105.98 meV/atom which is similar to the DFT's value of -101.00 meV/atom [30]. This model was used by Sluiter to find new ordered PdAu alloys ground state structures [30]. In this work, a truncated version of Sluiter's cluster expansion was used. This simplified model includes pair's interactions up to the third Next Nearest Neighbor (NNN) shell [30].

In order to test if the new truncated Cluster Expansion would be accurate enough, the critical temperature for phase change (order to disorder) was calculated. The Gibbs free energy was computed using:

$$\Delta G = \Delta H - T\Delta S \tag{2.16}$$

where ΔG is the change in free energy, ΔH is the change in internal enthalpy and ΔS is the change in entropy. ΔG will decrease with increasing temperature, making the disordered phase more stable at high temperatures. At ΔG = 0, the stable ordered phase changes to the disordered phase at temperature T_c (critical temperature).

This study used NVT-Monte Carlo to predict the formation of SRO in PdAu alloys [30]. The cluster models outlined above for interstitial H and the energy of PdAu alloys were combined to predict the formation of SRO and its effect on H solubility [30]. We used the NVT-Monte Carlo (NVT-MC) to simulate the effect of H in disordered alloys ($Pd_{96}Au_4$ and $Pd_{85}Au_{15}$) on the solubility of the alloys. The energy of the alloy structures were calculated with the truncated Cluster Expansion (4 clusters) which calculates the enthalphy of formation of the metal atoms. The binding energies in the O and T sites were calculated using the full Cluster Expansion used to calculate the binding energies of interstitial H in the metal atoms. The simulation consisted of introducing hydrogen in the metal membrane and letting the metal membrane equilibrate with the hydrogen adsorbed in the available interstitial sites through thermodynamic relaxation. The hydrogen was inserted with gaussian distribution adjusted for operating pressure:

$$probability = \frac{\exp(\frac{-E_i}{K_b T})}{\sum_i \exp(\frac{-E_i}{K_b T})} * \sqrt{P_{H_2}} \qquad (2.17)$$

where E_i is the binding energy of the interstitial site, K_b is Boltzmann constant and P_{H2} is the pressure of hydrogen. The pressure term was included in order to capture the change in the concentrations of hydrogen in the membrane due to the pressure of the H_2 gas. The system containing metal atoms and hydrogen was equilibrated using Metropolis acceptance rule with the energy of the system including the enthalpy of formation and the binding energies of hydrogen present in the alloy. At each NVT-MC step, two metal atoms were randomly swaped. The new structure enthalpy of formation was calculated and also the binding energies of H in the

interstitial sites. The moves reducing the total energies were accepted with probability of unity and the rest of the moves were accepted with probability of :

$$\exp(-\frac{1}{K_b T}(E_{new} - E_{old})) \tag{2.18}$$

where K_b is the Boltzmann constant, T is the temperature, E_{new} is the total energy of the new structure and E_{old} is the old total energy of the alloy structure.

The summary of the algorithm describing the NVT-MC is:

1. Create disordered metal membrane structure with desired composition.
2. Metropolis Monte Carlo to equilibrate the structure by swapping two random metal atoms: use enthalpy of formation of metal atoms (100 attempted moves/metal atoms).
3. Use equilibrated structure to calculate binding energy of interstitial sites and SRO parameter (α_1).
4. Load new hydrogen in interstitial sites using probability (Gaussian distribution adjusted for pressure). This step assumes that the previous load of H is removed before the insertion of new H.
5. Fix hydrogen position and calculate binding energy of inserted H.
6. Metropolis Monte Carlo to equilibrate system: use enthalpy of formation of metal atoms and binding energy of H (100 attempted moves/metal atoms).
7. Go to step 3 until system is saturated with H and final solubility is same as initial.

The pressure of H_2 was chosen so that the concentration of H at saturation still remains in the Sieverts' law range. In this study, all calculations with the lattice models outlined above were done with a structure made of 172 atoms with periodic boundary conditions. The calculations of

loading were repeated with 4000 atoms and the results were similar. In our calculation we assume that there were no crystal defects such as grain boundaries. In addition, the concentration of hydrogen being dilute, the average lattice constant of the alloy was presumed to remain constant in the presence of H [11].

CHAPTER 3: RESULTS

Lattice constants were optimized with DFT for the alloys used in the calculations without the presence of H. The lattice parameter was optimized using the 27 atom supercell containing the specific material composition. The initial estimations were done using Vegard's law [37]:

$$a_{PdAu} = X_{Pd} a_{Pd} + X_{Au} a_{Au} \tag{3.1}$$

Where a_{PdAu}, a_{Pd}, a_{Au} are the lattice constants for the fcc alloy, pure Pd, pure Au and X_{Pd}, X_{Au} are the atomic compositions of Pd and Au. Vegard's law is a linear approximation that is a good initial guess for the lattice constants for materials with the same crystal structure. The lattice parameters were computed over a range of values using increments of $\pm$ 0.01 Å. In order to reduce the computation time, the experimental lattice constants of the pure metals were used to estimate the lattice constant in Eq.(3.1). This approximation is an experimental lattice constant prediction. Hence, the DFT lattice constant could be calculated with:

$$a_{PdAu}{}^{DFT} = a_{Pd}{}^{DFT} + (a_{PdAu}{}^{\exp} - a_{Pd}{}^{\exp}) \tag{3.2}$$

where $a_{PdAu}{}^{\exp}$ is the prediction using experimental lattice parameters of the pure metals in Eq.(3.1), $a_{Pd}{}^{\exp}$ is the lattice parameter experimentally observed for pure Pd, and $a_{Pd}{}^{DFT}$ is the DFT calculated lattice parameter for pure Pd. In Table 1 data calculated by Sung Gu Kang is used to compare the results for the Vegard's Law lattice parameters using Eq.(28) and the DFT calculated values for PdAu alloys of interest. The PdAu alloys have a very good correlation between the predicted lattice constants and the DFT calculated values.

Table 1. Lattice constant comparison between DFT calculations for Pd-Au alloys and Vegard's Law, with lattice constants shown in Å.

Alloy composition	DFT lattice constant	Vegard's Law lattice constant
$Pd_{96}Au_4$	3.968	3.968
$Pd_{85}Au_{15}$	3.993	3.993

In Table 2 DFT data from Sung Gu Kang is used to compare the DFT optimized lattice constants with experimental values. There is less than two percent difference between the DFT and the experimental values.

Table 2. Lattice constant comparison between DFT calculations for Pd-Au alloys and experimental values at approximately the same compositions [35, 36]. Lattice constants are shown in Å.

	DFT optimized lattice constant	Experimental lattice constant	%difference
Pd	3.960	3.889	1.83
Pd96Au4	3.968	3.903	1.67
Pd85Au15	3.993	-	-

In order to test the Cluster Expansion, which calculates the binding energies of H in O and T sites, we plot the DFT data and the fitted CE model. This plot will be a visual aid to determine how well the CE model fits the DFT data. The predictions of the CE model for a randomly generated volume that represents a bulk alloy can also be compared to the set of sites in the DFT calculations. The sites examined in the DFT were selected using a characterization of counting the nearest-neighboring (NN) and next-to-nearest-neighboring metal atoms (NNN). A CE model is obtained by performing a least squares fit treating all sites equally. However, for the cumulative probability a relative weighting for each DFT site was determined differently. In a

random volume of the alloy sites were characterized by counting the number of Pd atoms in the shells surrounding the binding site up to the next-to-next-nearest-neighboring (NNNN) metal atom shell. Then, the probability of finding each site in the bulk of the random volume was computed. The DFT sites were characterized similarly for the O and T sites.

In Figure 2 [1] the cluster expansion binding energy calculations and the DFT calculations for $Pd_{85}Au_{15}$. O sites are represented by diamonds and T sites are the squares. The low standard deviation indicates an excellent fit between the CE model and the DFT data for the O and T sites. This agreement allowed us to proceed in examining the CE model for each binding site in a random volume of the $Pd_{85}Au_{15}$ alloy, as seen in Figure 3. It can been seen from Figure 3 that the CE model has not predicted any O or T sites with a lower binding energy than the sites calculated with DFT. A binding site with lower energy would signify that additional DFT calculations would be required because the lower energy sites dominate the H solubility. The cluster expansion parameters for $Pd_{96}Au_4$ were similarly analyzed and demonstrated the same agreement [13].

[1] The data in Figs. 2 and 3 and the cluster expansion used in these figures were developed by Sung Gu Kang.

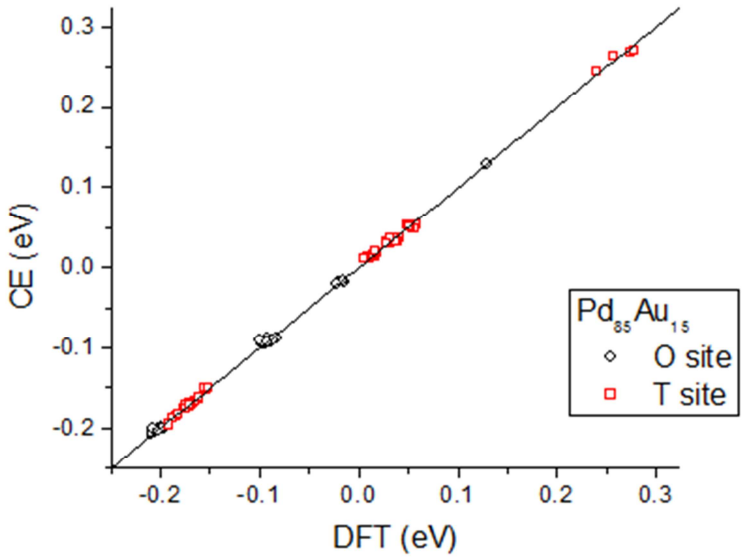

Figure 2. Cluster expansion for $Pd_{85}Au_{15}$. A comparison of the CE model and the DFT data binding energies. The O sites are represented by diamonds, squares represent T sites.

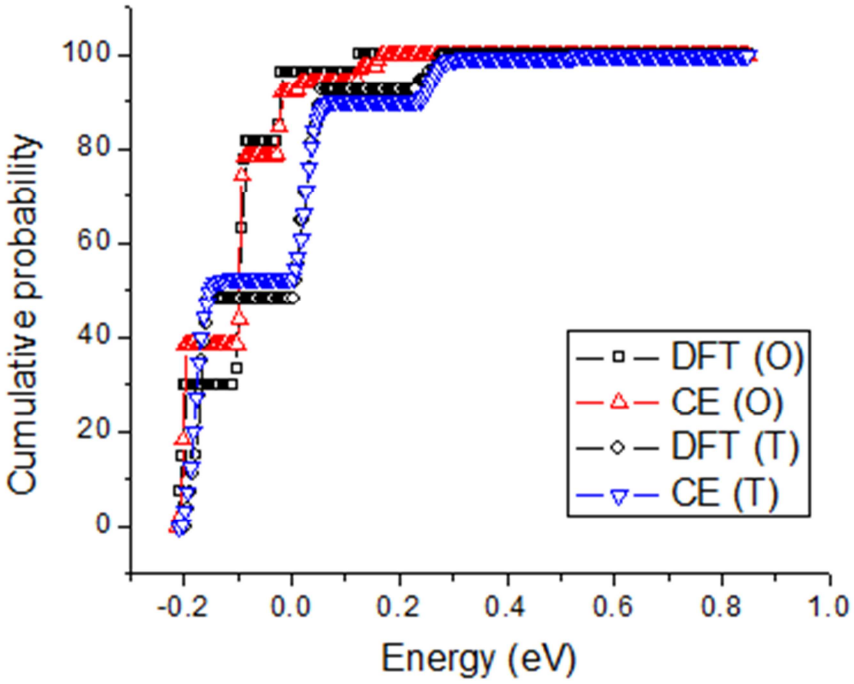

Figure 3. Cumulative probability for the DFT data and the CE model. Squares are DFT data and triangles are CE values.

Figure 4 shows the calculated equilibrium loading (H/M) for the pure Pd and two Pd alloys ($Pd_{85}Au_{15}$ and $Pd_{96}Au_4$) at temperatures ranging from 600 to 1200 K. We can observe that the loading increases with gold content in the alloy at each temperature. The experimental solubility value for pure Pd is lower than the predicted value by the model [4]. The model overestimated the loading significantly more at lower temperatures (T<800 K) but is more accurate at higher temperature (T>900 K). The reason for the difference between the experimental and model prediction can be explained by the fact that the cluster expansion was derived from the DFT calculations, which tend to slightly over predict the binding energies in the metals. Another factor in the difference is the error in the lattice parameter fitting. Finally, experimental results also include uncertainties due to the difficulty of obtaining reliable data at high temperatures.

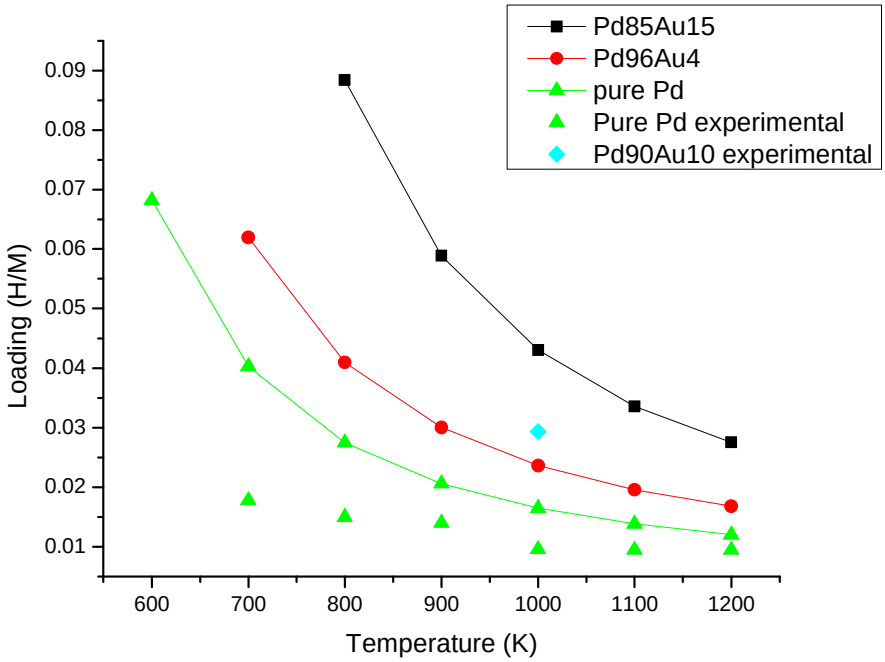

Figure 4. Loading (H/M) for Pd, $Pd_{85}Au_{15}$ and $Pd_{96}Au_4$ at 1 atm. The experimental results are from Refs. [4, 40].

Next, we calculated the SRO parameters, α_1, for different compositions of alloy. The system contained 4000 atoms and the calculations were repeated 10 times to calculate the standard deviation. In Table 3, the α_1 for the disordered $Pd_{50}Au_{50}$ alloy was calculated and was found to be approximately zero (0.0029 ± 0.0140). In addition, a two phase region was calculated with Pd and Au fully segregated and an α_1 of 0.78 ± 0.000173 was computed. The α_1 for the stoichiometric ordered phases, Pd_3Au and PdAu, were -0.333. The aim of these calculations was simply to verify that our calculations of the SRO parameters were performed correctly. Similar results were calculated by Kamakoti [11].

Table 3. SRO parameters for different compositions of PdAu alloys.

Structure	X_{pd}	SRO parameter: α_1	Standard deviation
$Pd_{50}Au_{50}$ (disordered)	0.50	0.0029	0.0140
$Pd_{75}Au_{25}$ (2 phases)	0.75	0.78	0.000173
Pd_3Au	0.75	-0.33	0
PdAu	0.50	-0.33	0

In Figure 5, we plotted the loading (H/M) as a function of the Short Range Order parameter (α_1) for the $Pd_{85}Au_{15}$ alloy at different temperatures (900 to 1200K) and an H_2 pressure of 1 atm. In these calculations, the partially ordered alloy structures were generated using Reverse Monte Carlo and the metal structure was not changed in any way by the presence of H. The range of temperatures was chosen in order for the loading to be in the valid region (loading <0.1). At 900 K, we observe that the loading increases with α_1 becoming positive. Hence, the loading increases with clustering or segregation of the two metal atoms in different

phases. The increase in loading is due to the increase in more preferable interstitial sites in the Pd phase. This effect is seen at 1000, 1100 and 1200 K. In Table 4, we calculated the standard deviation of the loading for the alloy at different SRO parameters and temperatures by repeating the loading calculations 10 times for the same structure with a specific α_1.

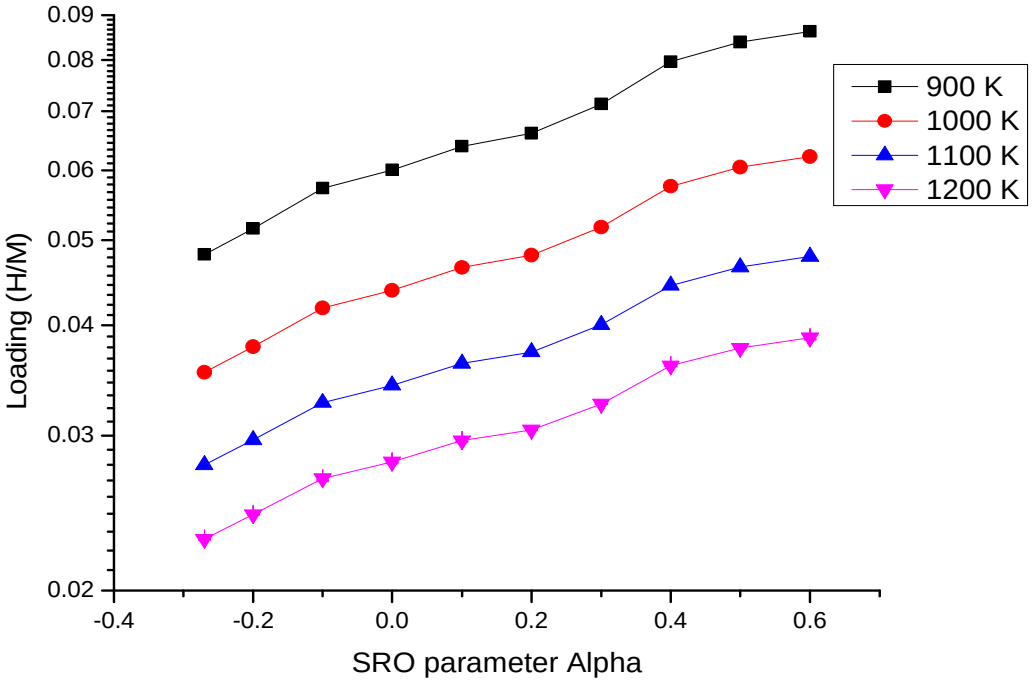

Figure 5. *Loading (H/M) as a function of Short Range Order parameter (α_1) at 1 atm for $Pd_{85}Au_{15}$ alloy.*

Table 4. $Pd_{85}Au_{15}$ loading standard deviation

α_1 / T(K)	-0.27	-0.2	-0.1	0	0.1	0.2	0.3	0.4	0.5	0.6
900	7.88E-05	4.54E-05	2.23E-04	1.47E-04	1.32E-04	0.00E+0	1.39E-17	5.61E-05	0.00E+0	2.27E-04
1000	5.35E-05	3.23E-05	1.60E-04	1.05E-04	9.32E-05	6.94E-18	0.00E+0	3.78E-05	6.94E-18	1.60E-04
1100	3.89E-05	2.45E-05	1.23E-04	8.06E-05	7.02E-05	6.94E-18	6.94E-18	2.73E-05	6.94E-18	1.20E-04
1200	2.98E-05	1.96E-05	9.88E-05	6.46E-05	5.56E-05	3.47E-18	6.94E-18	2.08E-05	0.00E+0	9.55E-05

In Figure 6, we plotted the loading (H/M) as a function of the Short Range Order parameter (α_1) for the $Pd_{85}Au_{15}$ alloy at different temperatures (700 to 1200K) and a pressure of 1 atm. The range of temperatures was chosen in order for the loading to be in the valid region (loading <0.1). At 700 K and 800 K, we observe that the loading increases with α_1 becoming positive. Hence, the loading increases with clustering. The loading remains constant at varying SRO parameters for 900, 1000, 1100 and 1200 K. In Table 5, we calculated the standard deviation of the loading for the alloy at different SRO parameters and temperatures by repeating the loading calculations 10 times for the same structure with a specific α_1.

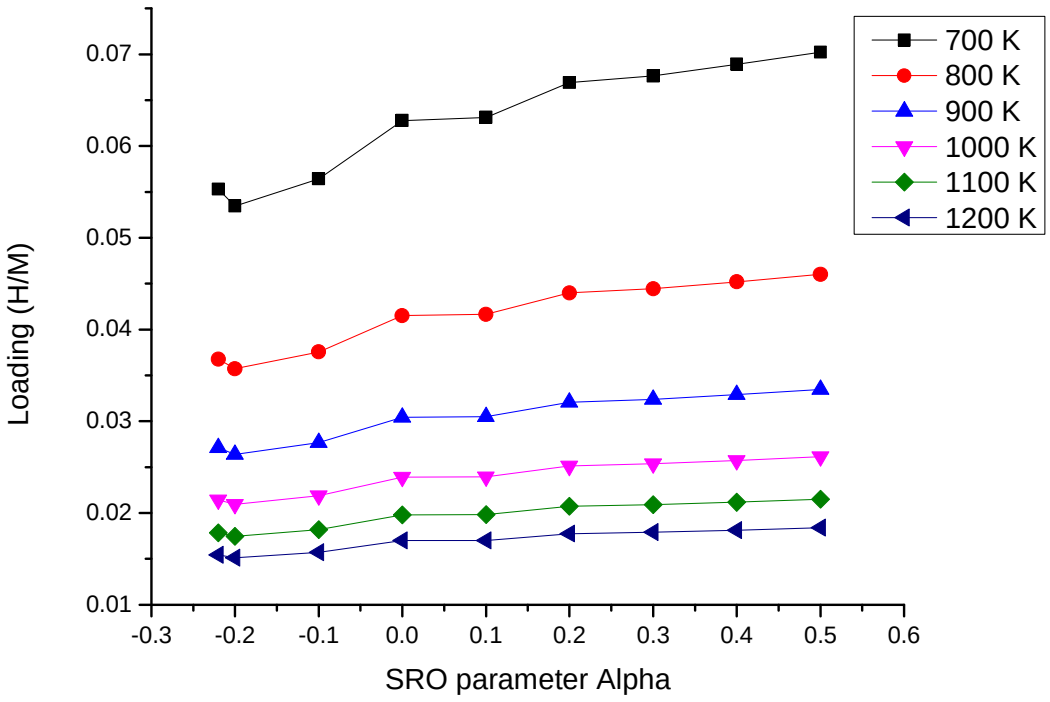

Figure 6. Loading (H/M) as a function of Short Range Order parameter (α_1) at 1 atm for $Pd_{96}Au_4$ alloy.

Table 5. $Pd_{96}Au_4$ loading standard deviation.

α_1 / T(K)	-0.22	-0.2	-0.1	0	0.1	0.2	0.3	0.4	0.5
700	8.52E-05	8.87E-05	2.91E-04	6.15E-04	1.39E-17	1.39E-17	6.15E-04	4.82E-04	3.53E-04
800	7.21E-05	5.61E-05	1.80E-04	3.79E-04	0.00E+00	6.94E-18	3.85E-04	3.02E-04	2.22E-04
900	5.66E-05	3.90E-05	1.24E-04	2.61E-04	3.47E-18	6.94E-18	2.68E-04	2.11E-04	1.56E-04
1000	4.26E-05	2.89E-05	9.26E-05	1.94E-04	3.47E-18	3.47E-18	2.02E-04	1.60E-04	1.18E-04
1100	3.03E-05	2.22E-05	7.34E-05	1.52E-04	3.47E-18	0.00E+00	1.60E-04	1.27E-04	9.42E-05
1200	1.94E-05	1.75E-05	6.07E-05	1.25E-04	3.47E-18	0.00E+00	1.32E-04	1.06E-04	7.84E-05

In Figure 7, we plotted the diffusivity of pure Pd and $Pd_{96}Au_4$ alloy. The binding energies in the alloy were calculated using the cluster expansion developed by Semidey to calculate the O, T and Transition States (TS) binding sites. The Kinetic Monte Carlo was used to computed the mean square displacement and the diffusivity. The pure palladium's diffusivity is in good agreement with the experimental results [42].

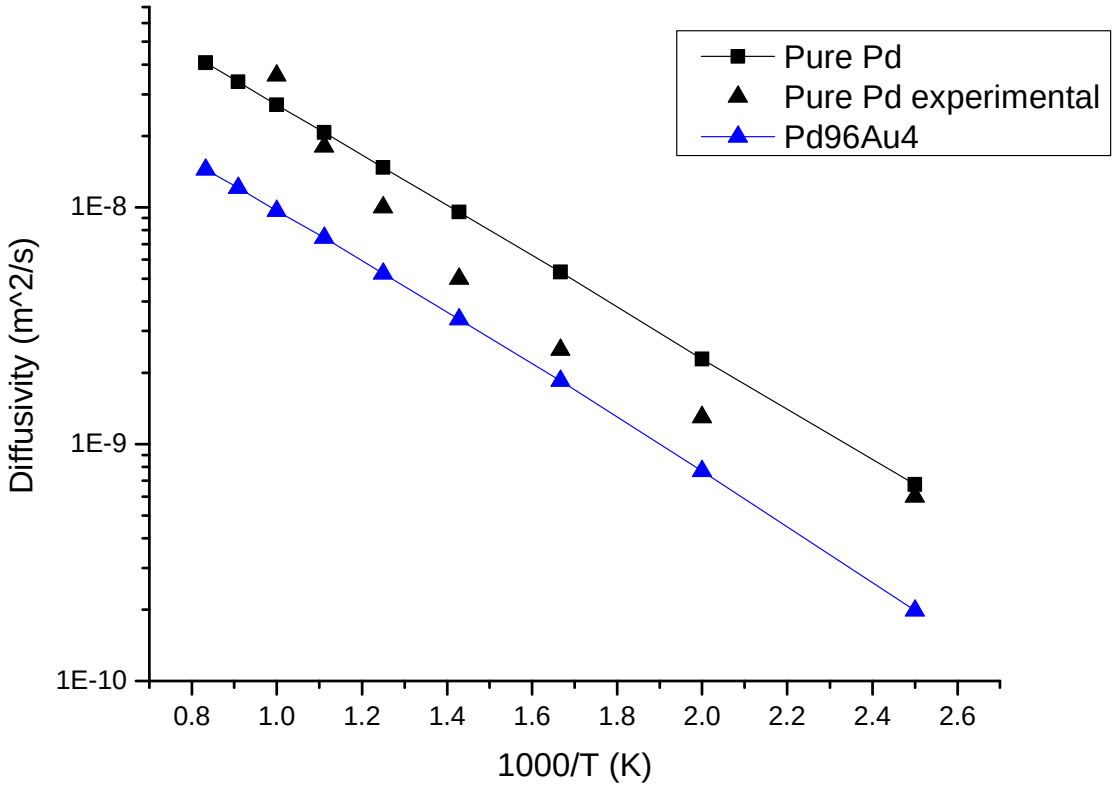

Figure 7. Diffusivity of pure Pd and $Pd_{96}Au_4$ alloys as a function of Temperature. Experimental results from Ref. [42].

In Figure 8, we plotted the permeability of pure Pd and $Pd_{96}Au_4$ alloy. The pure Pd values are in good agreement agree with experimental results for high temperatures (T >1000 K). However, for lower temperatures there is a large dissimilarity. This might be because the solubility and diffusivity calculations both are approximation calculations. The combination of the errors from those two calculations will compile in the permeability calculation. The experimental permeability of the $Pd_{90}Au_{10}$ alloy at 333.33 K [40] is in good agreement with the calculated permeability of $Pd_{96}Au_4$.

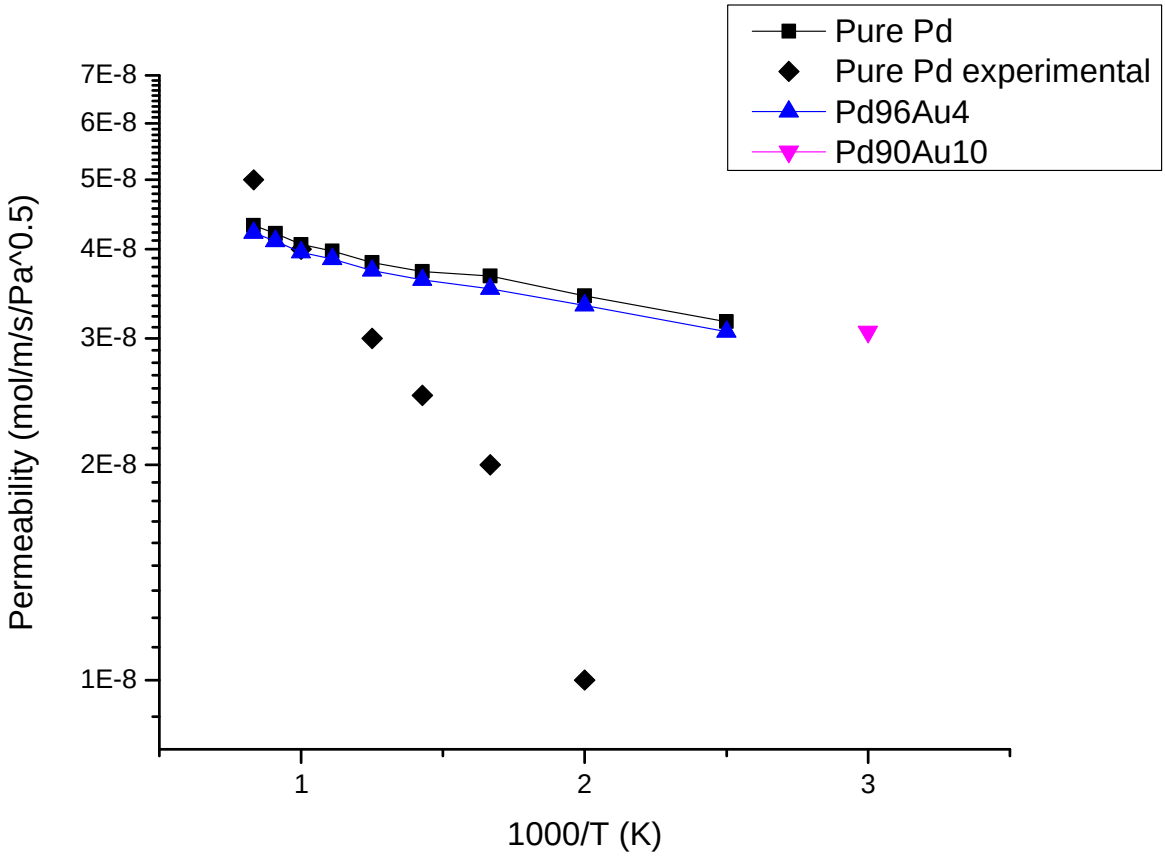

Figure 8. Permeability Pd and $Pd_{96}Au_4$ alloy. Experimental results are from [40, 43-50].

As previously mentioned we used a cluster expansion to calculate the enthalpy of formation of the metal atoms present in the system. The original cluster expansion used 23 clusters and sub clusters. In our work we used 4 clusters including two body interactions at the nearest neighbors and next nearest neighbors. We calculated the critical temperature at which the alloy structure changes from ordered to disorder for the $Pd_{50}Au_{50}$ alloy, which has a L_{10} ordered structure (layered structure). The critical temperature of 423 K was found using the 23 clusters. This result is close to the experimental value of 373 K [41]. The calculated critical temperature

value is 97 K using the truncated cluster expansion. The truncated cluster expansion's critical temperature is considerably lower than the full cluster's result. Nevertheless, we used the truncated cluster expansion in our calculations for simplicity. It may be desirable in future work to include all the terms from Sluiter's cluster expansion.

In the next part, we used the NVT –Monte Carlo algorithm described earlier to observe the effect of the introduction of hydrogen on the structure and on the solubility of the metal alloy membranes. We choose pressures in order to stay within the Sieverts' law. As a reminder, an iteration consists of the equilibration of the metal atoms of the alloy after the insertion of new hydrogen in the interstitial sites. The hydrogen atoms are introduced from iteration 1. The iteration 0 is the result of the metal atoms equilibration without hydrogen absorbed. The plot in Figure 9 is the SRO parameter (α_1) as a function of iterations for the $Pd_{94}Au_4$ alloy at 400 K and a pressure of 0.01 atm. We can observe that structure does change when the presence of H is considered. The standard deviation on the α_1 was calculated from the computational tests done previously on 10 randomly generated structures. The SRO parameter initially at the disordered structure value of zero changed to a SRO parameter of -0.08 $\pm$ 0.014. We plotted in Figure 11 the change in loading after each insertion of hydrogen in the metal membrane. The loading fluctuated around the saturation level at each iteration.

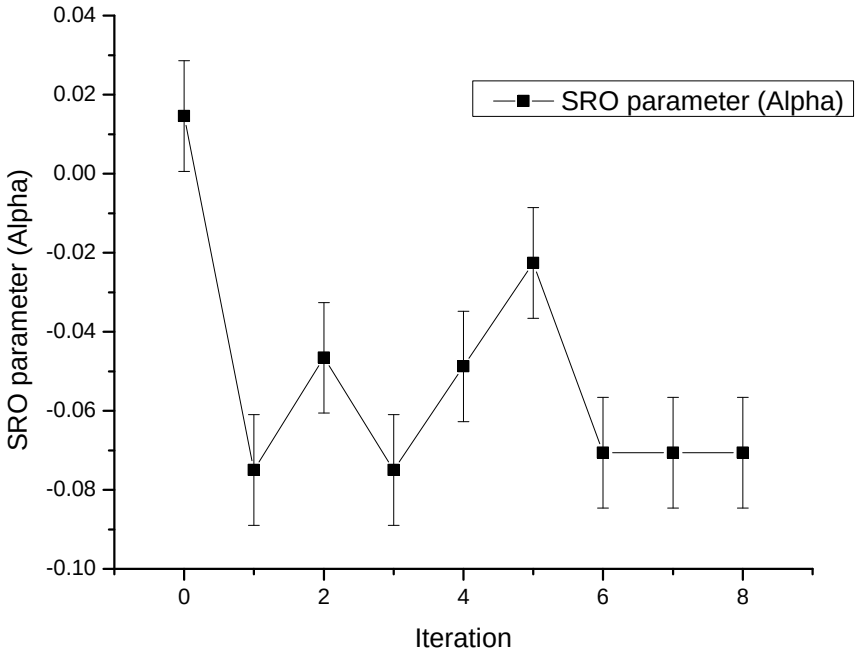

Figure 9. SRO parameter (α_1) for $Pd_{96}Au_4$ at 400 K and P=0.01 atm.

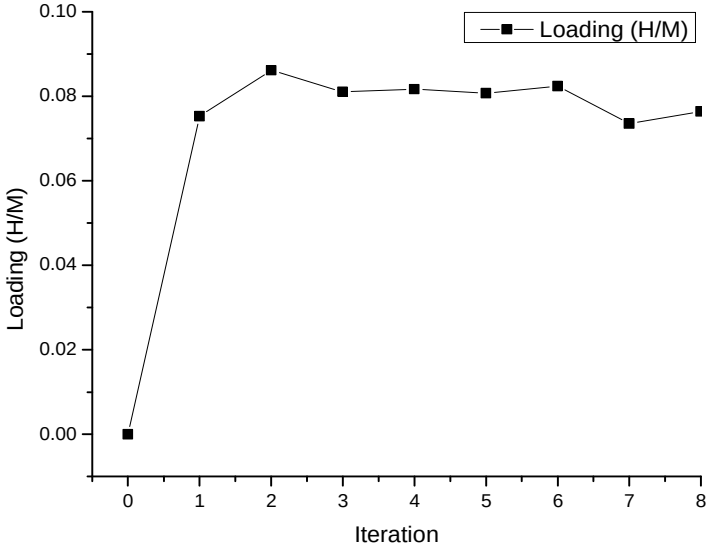

Figure 10. Loading (H/M) for $Pd_{96}Au_4$ at 400 K and P=0.01 atm.

We also performed similar calculations on $Pd_{85}Au_{15}$ at 1000 K and 3 atm. Figure 14 is the plot of the SRO parameter (α_1). The standard deviation was also taken from the 10 disordered structures generated previously. We can observe that structure does change significantly. The SRO parameter starts at the disordered structure value of zero and changes to a value of -0.05 $\pm$ 0.014. In Figure 15, we plotted the change in loading after each insertion of hydrogen in the metal membrane. The loading fluctuated around the saturation level at each iteration.

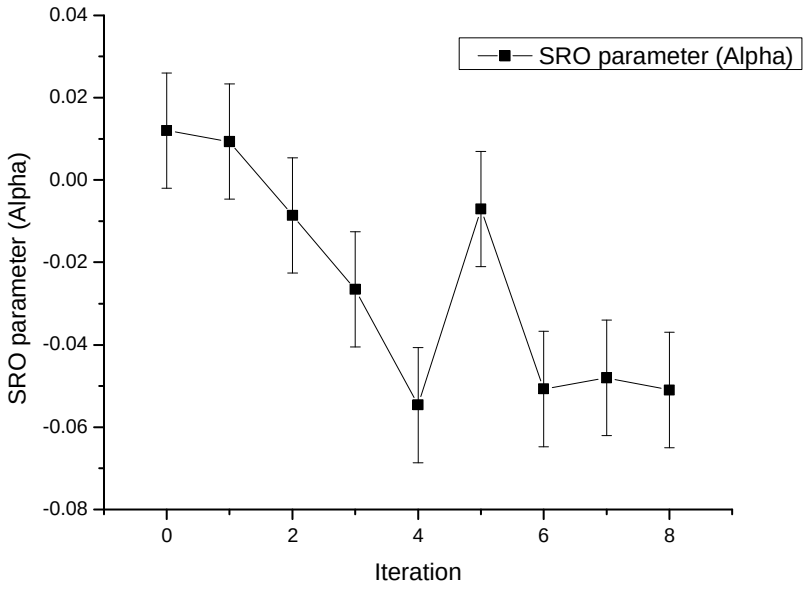

Figure 11. SRO parameter as a function of iteration of hydrogen insertion in $Pd_{85}Au_{15}$ at 500 K and P=3 atm.

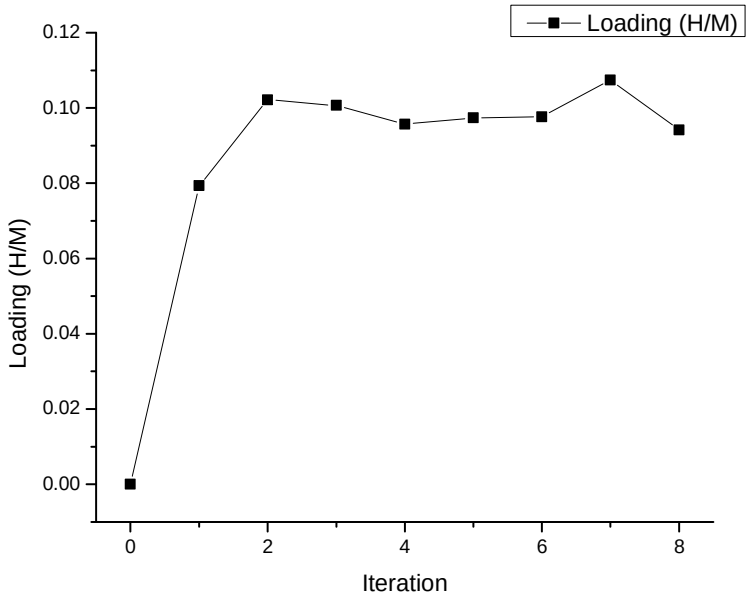

Figure 12. Loading of hydrogen in $Pd_{85}Au_{15}$ at 500 K and P=3 atm.

CHAPTER 4: CONCLUSION

We used NVT-Monte Carlo with fixed number of atoms, fixed simulation volume and temperature to analyze the effect of hydrogen in metal alloy membranes. Hydrogen was introduced in the metal membrane at each iteration and the metal membrane with hydrogen was brought to equilibrium. Before each insertion of hydrogen, the previous load of hydrogen was removed from the metal membrane interstitial sites. We observed that the $Pd_{96}Au_4$ at 400 K and 0.01 atm had the structural change from disordered to SRO. The SRO parameter (α_1) changed from ~0 to -0.08 $\pm$ 0.014. The loading (H/M) reached the saturation level at each iteration.

Similarly for $Pd_{85}Au_{15}$ at 1000 K and 3 atm the fcc crystal structure changed from the substitutionally disordered alloy ($\alpha_1 \sim 0$) to an alloy with Short Range Ordering (α_1 = -0.05 $\pm$ 0.014). The loading (H/M) remained constant around 0.1 H/M. Finally, we have successfully demonstrated that as seen in experiment the presence of hydrogen in a metal alloy membrane will change the structure from disorder to order or specifically SRO. The loading reached the saturation level at each iteration.

The results from this work can help experimentalists who can use the temperatures and pressures used in the simulation at which the structure of the alloys changed from disordered to SRO. At higher hydrogen pressures and lower temperatures the change in structure will be more pronounced and loading will increase with the formation of SRO.

The NVT-Monte Carlo can be applied to the diffusivity calculation in order to calculate how hydrogen presence can influence the diffusion of hydrogen in the metal membrane. This calculation will allow for the calculation of the effect of hydrogen on the permeability or flux of

hydrogen in the alloy. In addition, a cluster expansion with more accuracy for the calculations of binding energies of interstitial sites and enthalpy of formation of metal atoms could be used. Finally, once a cluster expansion is developed for other metal alloy this method can be used to investigate the effect of hydrogen on the performance of those alloys.

Appendix A: O CLUSTER EXPANSION PARAMETERS DESCRIPTION AND VALUES FOR $Pd_{96}Au_4$

Table 6. O Site Cluster Expansion description for $Pd_{96}Au_4$ [13].

Parameter ID #:	Description
1	Number of Pd atoms in the 2 x N shell normalized by 2
2	Number of Pd atoms in the 3 x N shell normalized by 3
3	Number of Cu (M in the case of the binary alloys) atoms in the 2 x N shell normalized by 2
4	Number of Cu (M in the case of the binary alloys) atoms in the 3 x N shell normalized by 3
5	Number of M (in the ternary alloys) atoms in the 2 x N shell normalized by 2
6	Number of M (in the ternary alloys) atoms in the 3 x N shell normalized by 3
7	2 body interactions between metal atoms separated by L/sqrt(2) in the 2 x N shell normalized by L/sqrt(2)
8	2 body interactions between metal atoms separated by L in the 2 x N shell normalized by L
9	2 body interactions between metal atoms separated by L in the 3 x N shell normalized by L
10	2 body interactions between metal atoms separated by sqrt(2)*L in the 3 x N shell normalized by sqrt(2)*L
11	2 body interactions between metal atoms separated by sqrt(3)*L in the 3 x N shell normalized by sqrt(3)*L
12	2 body interactions between metal atoms in the 2 x N shell separated by L/sqrt(2) to atoms in the 3 x N shell normalized by L/sqrt(2)
13	3 body interactions between metal atoms in the 2 x N shell where each atom is separated by L/sqrt(2) normalized by L/sqrt(2)
14	3 body interactions between metal atoms in the 3 x N shell where each atom is separated by Lnormalized by L
15	4 body interactions between metal atoms in the 2 x N shell where each atom is separated by L/sqrt(2) normalized by 2
16	4 body interactions between metal atoms in the 3 x N shell where each atom is separated by sqrt(2) *L normalized by 3
17	Number of Pd atoms in the 4 x N shell normalized by 4
18	Number of Cu (M in the binary alloys) atoms in the 4 x N shell normalized by 4
19	Number of M (in ternary alloys) atoms in the 4 x N shell normalized by 4
20	Number of Pd atoms in the 5 x N shell normalized by 5

Table 7. $Pd_{96}Au_4$ O site binding energies and ZPE in eV [13].

	E_b	ZPE
E_o	0.7067	0.9206
1	0.3194	0.2929
2	-	-
3	-	-0.2296
4	0.0325	-
5	-	-
6	-	-
7	-	0.0169
8	0.1510	-0.0541
9	-	-
10	-	-
11	-	-
12	-	-
13	-	-
14	-	-
15	-	-
16	-	-
17	-	-
18	-	-
19	-	-
20	-	-

Appendix B: T CLUSTER EXPANSION PARAMETERS DESCRIPTON AND VALUES FOR $Pd_{96}Au_4$

Table 8. T site Cluster Expansion parameters description for $Pd_{96}Au_4$ [13].

Parameter ID #:	Description
1	Number of Pd atoms in the 2 x N shell normalized by 2
2	Number of Pd atoms in the 3 x N shell normalized by 3
3	Number of Cu (M in the case of the binary alloys) atoms in the 2 x N shell normalized by 2
4	Number of Cu (M in the case of the binary alloys) atoms in the 3 x N shell normalized by 3
5	Number of M (in the ternary alloys) atoms in the 2 x N shell normalized by 2
6	Number of M (in the ternary alloys) atoms in the 3 x N shell normalized by 3
7	2 body interactions between metal atoms separated by L/sqrt(2) in the 2 x N shell normalized by L/sqrt(2)
8	2 body interactions between metal atoms separated by L/sqrt(2) in the 3x N shell normalized by L/sqrt(2)
9	2 body interactions between metal atoms separated by (sqrt(6)*L)/2 in the 3 x N shell normalized by (sqrt(6)*L)/2
10	2 body interactions between metal atoms separated by sqrt(2)*L in the 3 x N shell normalized by sqrt(2)*L
11	2 body interactions between metal atoms separated by (sqrt(10)*L) /2 in the 3 x N shell normalized by (sqrt(10)*L)/2
12	2 body interactions between metal atoms in the 2 x N shell separated by L/sqrt(2) to atoms in the 3 x N shell normalized by L/sqrt(2)
13	2 body interactions between metal atoms in the 2 x N shell separated by L to atoms in the 3 x N shell normalized by L
14	2 body interactions between metal atoms in the 2 x N shell separated by(sqrt(6)*L)/2 to atoms in the 3 x N shell normalized by (sqrt(6)*L)/2
15	Number of Pd atoms in the 4 N shell normalized by 4
16	Number of Cu (M in the binary alloys) atoms in the 4 x N shell normalized by 4
17	Number of M (in ternary alloys) atoms in the 4 x N shell normalized by 4
18	2 body interactions between metal atoms separated by L/sqrt(2) in the 4 x N shell normalized by L/sqrt(2)
19	2 body interactions between metal atoms in the 3 x N shell separated by L/sqrt(2) to atoms in the 4 x N shell normalized by L/sqrt(2)
20	2 body interactions between metal atoms in the 2 x N shell separated by L to atoms in the 4 x N shell normalized by L
21	Number of Pd atoms in the 5 N shell normalized by 5
22	Number of Cu (M in the binary alloys) atoms in the 5 x N shell normalized by 5

Table 8 (Cont.). T site Cluster Expansion parameters description for $Pd_{96}Au_4$ [13].

23	Number of M (in ternary alloys) atoms in the 5 x N shell normalized by 5
24	3 body interactions between metal atoms in the 2 x N shell separated by L/sqrt(2) normalized by L/sqrt(2)
25	3 body interactions between metal to metal atoms separated by L/sqrt(2) in the 2 x N shell to atoms in the 3 x N shell separated by L/sqrt(2) normalized by L/sqrt(2)
26	3 body interactions between metal atoms in the 3 x N shell separated by L/sqrt(2) normalized by L/sqrt(2)
27	3 body interactions between two metal atoms separated by L/sqrt(2) in the 3 x N shell to atoms in the the 2 x N shell separated by L/sqrt(2) normalized by L/sqrt(2)
28	3 body interactions between two metal atoms separated by (sqrt(6)*L)/2 in the 3 x N shell to atoms in the the 2 x N shell separated by L/sqrt(2) normalized by (sqrt(6)*L)/2
29	3 body interactions between metal atoms in the 4 x N shell separated by L/sqrt(2) normalized by L/sqrt(2)
30	3 body interactions between two metal atoms separated by L/sqrt(2) in the 3 x N shell to atoms in the the 4 x N shell separated by L/sqrt(2) normalized by L/sqrt(2)

Table 9. $Pd_{96}Au_4$ T site binding energies and ZPE in eV [13].

	E_b	ZPE
E_o	0.8591	0.1960
1	0.5054	0.0100
2	-	-
3	-	-
4	-	-
5	-	-
6	-	-
7	0.0086	0.0043
8	-	-
9	-	-
10	-	-
11	-0.0040	-
12	-	-
13	0.0260	-
14	-0.0056	0.0012
15	-	-
16	-	-
17	-	-
18	-	-
19	-0.0005	-
20	-0.0019	-0.0013
21	-	-
22	-	-
23	-	-
24	-	-
25	-	-
26	-	-
27	-	-
28	-	-
29	-	-
30	-	-

Appendix C: TS CLUSTER EXPANSION PARAMETERS VALUES FOR $Pd_{96}Au_4$

Table 10. $Pd_{96}Au_4$ TS sites binding and ZP energy in eV [13].

	E_b	ZPE
E_o	1.4747	0.2027
O 1	-	-0.0044
O 2	-	-
O 3	-	-
O 4	-	-
O 5	-	-
O 6	-	-
O 7	-	-
O 8	-	-
O 9	-	-
O 10	-	-
O 11	-	-
O 12	-0.0081	-
O 13	-	-
O 14	-	-
O 15	-	-
O 16	-	-
O 17	-	-
O 18	-	-
O 19	-	-
O 20	-	-
T 1	0.4336	0.0170
T 2	-	0.0070
T 3	-	-
T 4	-	-
T 5	-	-
T 6	-	-
T 7	-	-
T 8	-	-0.0009
T 9	-0.0360	-
T 10	-	0.0024
T 11	-	-
T 12	-	0.009

Table 10 (Cont.). Pd96Au4 TS sites binding and ZP energy in Ev [13].

T 13	-	-
T 14	-	0.0022
T 15	0.2455	0.0013
T 16	-	-
T 17	-	-
T 18	-	-
T 19	-	-
T 20	0.0665	-
T 21	-	-
T 22	-	-
T 23	-	-
T 24	-	-
T 25	-	-
T 26	-	-
T 27	-	-
T 28	-	-
T 29	-	-
T 30	-	-

Appendix D: O AND T CLUSER EXPANSION PARAMETERS VALUES FOR $Pd_{85}Au_{15}$

Table 11. $Pd_{85}Au_{15}$ O and T site binding and ZP energy in eV.

O-parameters	E_b (eV)	ZPE (ev)
Eo	-0.09945	0.003819
1	0.035259	0.055231
2	0	0
3	0.14912	0.238698
4	0	0
5	0	0
6	0	0
7	-0.02539	0.047868
8	0.111957	0.002445
9	0	0
10	0	0
11	0	0
12	0	0
13	0	0
14	0	0
15	0	0
16	0	0
17	-0.00561	-0.0039
18	0	0
19	0	0
20	0	0

Table 12. $Pd_{85}Au_{15}$ O and T site binding and ZP energy in eV.

T-parameters	E_b (eV)	ZPE (ev)
Eo	0.8914384	0.1912565
1	0.4974388	0.004870067
2	0	0
3	0	0
4	0	0
5	0	0
6	0	0
7	0.02086105	0.004612865
8	0	0
9	0	0
10	0	0
11	0	0
12	0	0
13	0	0
14	0	0
15	0.045099996	0.003951982
16	0	0
17	0	0
18	0	0
19	0	0
20	0	0
21	0	0
22	0.010508769	-0.000329031
23	0	0
24	0	0
25	0	0
26	0.002841875	0.00017404
27	0	0
28	0.0015445	0.000040807
29	0	0
30	0	0

APPENDIX E: PERMEABILITY CONVERSION

In order to compare the calculated permeability with experimental values k (m^2 $atm^{-0.5}$ /s) needs to be converted to mol/m/s/$Pa^{0.5}$ [3]. Sieverts' law will be used with the H concentration, C_H (mol/m^3) instead of the loading and P_{H2} will be in Pascals:

$$C_H = K_s^* P_{H_2}^{0.5}$$

where K_s* is in mol/m^3/$Pa^{-0.5}$ [3] . The modified K_s* can be obtained by:

$$K_s^* = \frac{K_s}{318.3 V_m}$$

where Ks is the unmodified Siervert's constant in $atm^{-0.5}$, and Vm is the molar volume occupied by the alloy in m^3/mol (Vm= $8.86*10^{-6}$ m^3/mol for pure Pd having a lattice constant of 3.89 Angstrom) and 318.3 is a factor representing the conversion from $atm^{-0.5}$ to $Pa^{-0.5}$ [11].

APPENDIX F: CLUSTER EXPANSION PARAMETERS TO CALCULATE THE ENTHALPY OF FORMATION OF PALLADIUM GOLD ALLOY: $Pd_{50}Au_{50}$ ordered L_{10} STRUCTURE AND DISORDERED

Table 13. L_{10} $Pd_{50}Au_{50}$ Cluster Expansion parameters.

Cluster number	Number of pure Pd clusters that occur in L_{10}, per AuPd formula unit	Total number of clusters of each type that occurs per AuPd formula unit	Correlation function	Effective Cluster Interaction (ECI) (meV/atom)	Contribution to enthalpy (meV/atom)
0	1	1	1	1.5929257	1.5929257
1	1	2	0.5	-198.771428	-99.385714
2	3	6	0.5	-58.9353281	-29.46766405
3	4	24	0.166666667	-33.9308377	-5.655139617
4	2	12	0.166666667	-99.8347017	-16.63911695

Enthalpy of formation (4 clusters) = -149.555 meV/atom.

Enthalpy of formation (23 clusters) = -105.982 meV/atom.

Table 14. Disordered $Pd_{50}Au_{50}$ Cluster Expansion parameters.

Cluster number	Correlation function	Effective Cluster Interaction (ECI)	Contribution to enthalpy
0	1	1.5929257	1.5929257
1	0.5	-198.771428	-99.385714
2	0.25	-58.9353281	-14.73383203
3	0.25	-33.9308377	-8.482709425
4	0.25	-99.8347017	-24.95867543

Enthalpy of formation (4 clusters) = -145.968 mev/atom

Enthalpy of formation (23 clusters) = -82.787 meV/atom

REFERENCES

1. Ockwig, N. W.; Nenoff, T. M., Membranes for Hydrogen Separation. *Chemical Review* **2007**, 107, 4078-4110.
2. Phair W.J., *et al*., Developments and Design of Novel (Non-Palladium-Based) Metal Membranes for Hydrogen Separation. *Ind. Eng. Chem. Res.* **2006**, 45, 5657-5674.
3. Chao, H. C., The effect of H_2S on the performance of Pd and Pd/Au composite membrane, *Journal of Membrane Scienc*e **2010,** 362, 535-544.
4. Kamakoti P.; Sholl, D. S., Prediction of Hydrogen Flux through Sulfur-Tolerant Binary Alloy Membranes. *Science* **2005**, 307, 569.
5. Kulprathipanja, A., *et .al*. Pd and Pd–Cu membranes: inhibition of H2 permeation by H_2S. *Journal of Membrane Science* **2005**, 254, 49-62.
6. Lee, S. M., *et al*., Hydrogen-induced lattice rearrangement of a $Pd_{0.81}Au_{0.19}$ alloy. *Journal of Physics: Condensed Matter* **2007**, 18 (19), 326222.
7. Flanagan, T.B., *et al.*, Hydrogen in Disordered and Ordered Palladium Alloys, *Platinum Metals Review* **1993**, 1, 37.
8. Flanagan, T. B., et al., A possible role for hydrogen-induced lattice migration in alloy materials processing, *Journal of Alloys and Compounds* **1995**, 231, 1-9.
9. Sonwane, C. G., *et al*., Achieving optimum hydrogen permeability in PdAg and PdAu alloys. *The Journal of Chemical Physics* **2006**, 125, 184714.
10. Lei, S.; Goldbach, A.; Zeng, G.; Xu, H., Preparation and performance of thin-layered PdAu/ceramic composite membranes, *International journal of hydrogen energy* **2010,** (35), 420, 1–4208.
11. Kamakoti, P.; Sholl, D. S., Ab initio lattice-gas modeling of interstitial hydrogen diffusion in CuPd alloys. *Physical Review B,* **2005**, 71, 014301.
12. Okamoto, H.; Massalski, T. B., *Binary Alloy Phase Diagrams*, 2nd ed., edited by T. B. Massalski *ASM International,* Materials Park, Ohio **1990**, Vol. 1, pp. 409-410.
13. Semidey-F. L.; Sholl D. S., Combining Density Functional Theory and Cluster Expansion Methods to Predict H2 Permeance Through Pd-Based Binary Alloy Membranes, *J. Chem. Phys.* **2008**, 128,144701.
14. Sluiter, M. H. F, Ab initio calculation of the phase stability in Au-Pd and Ag-Pt alloys, *Physical Review B* **2006,** 73, 174204.
15. Kamakoti, P.; Sholl, D.S., Ab Initio based Lattice Gas Modeling of Interstitial Hydrogen Diffusion in CuPd Alloys. *Phys. Rev. B*, **2005**, 71,014301.
16. Shiqiang, H.; Sholl, D. S., Computational prediction of durable amorphous metal membranes for H2 purification. *Journal of Membrane Science*, **2011**, 381, 192-196.

17. Shiqiang, H.; David S. S., Comparison of first principles calculations and experiments for hydrogen permeation through amorphous ZrNi and ZrNiNb films. *J. Membr. Sci.* **2010,** 350, 402-409.
18. Matsuo, Y.; Nagasawa A., Kakinoki J., Ordered alloys of the gold-palladium system. II. Electron diffraction study on Evaporated AuPd3 films. *J. of the Phys. Soc. of Jap.*, **1966**, 21, 12.
19. Nagasawa, A.; Matsuo, Y.; Kakinoki, J.; Ordered Alloys of Gold-Palladium System. I. Electron Diffraction Study of Evaporated Au3Pd Films. *J. of the Phys. Soc. of Jap.*, **1965**, (20), 1881-1885.
20. Iveronovna, V. I.; Katsnelson, A. A., *Sov. Phys. Crystallogr*., **1964**, (9), 467.
21. Ling, C.; Sholl D.S.; Using first-principles calculations to predict surface resistances to H_2 transport through metal alloy membranes. *J. Membr. Sci*., **2007**, 303, 162.
22. Šljivančanin, K.; Hammera, B., Oxygen dissociation at close-packed Pt terraces, Pt steps, and Ag-covered Pt steps studied with density functional theory. *Surface Science, **2002**, 515 (1), 235-244.*
23. Løvvik, O. M.; Olsen, R. A., Adsorption energies and ordered structures of hydrogen on Pd(111) from density-functional periodic calculations, *Physical Review B* **1998**, 16 (58), 10890-10898.
24. Løvvik, O. M.; Olsen, R. A., Density functional calculations on hydrogen in palladium–silver alloys, *Journal of Alloys and Compounds **2002,*** 330-332, 332-337
25. Gross, A.; Scheffler, M., Ab initio quantum and molecular dynamics of the dissociative adsorption of hydrogen on Pd(100), *Physical Review B* **1998**, 57, 2493-2506.
26. Gross, A.; Wilke, S.; Scheffler, M., Six-Dimensional Quantum Dynamics of Adsorption and Desorption of H2 at Pd(100): Steering and Steric Effects, *Physical Review letters* **1995**, 75, 2718-2721.
27. Elsässer, C.; Ho, K. M.; Chan, C. T.; Fähnle, M., Vibrational states for hydrogen in palladium, *Physical Review B* **1991**, 44, 10377-10380.
28. Elsasser, C.; Ho K. M.; Chan, C. T.; Fahnle, M., First-principles pseudopotential calculations for hydrogen in 4d transition metals. II. Vibrational states for interstitial hydrogen isotopes, *J. Phys.: Condens. Matter* **1992**, 4, 5207.
29. Cowley J.M., An approximation theory of order in alloys, *Physical Review* **1950**, 77 (5), 669.
30. Sluiter M., Ab initio calculation of the phase stability in Au-Pd and Ag-Pt alloys, Physical *Review B* **2006**, 73, 174204.
31. Sholl D.S, Steckel J, Density Functional Theory: A Practical Introduction, *John Wiley & Sons* **2008**, 43-200.
32. VASP, http://www.vasp.at/.
33. Perdew, J. P.; Chevary, J. A.; Vosko, S. H.; Koblar, A. J.; Pederson, M. R.; Singh, D. J.; Fiolhais C., *Physical Review B* **1992**, 46 (11), 6671-6687.

34. Chen, C. H.; Ma, Y. H., The effect of H2S on the performance of Pd and Pd/Au composite membrane, *Journal of Membrane Science* **2010,** 362, 535-544.
35. Sakamoto, Y.; Ohira, K.; Ishimarua, N.; Chen F.L.; Kokubu, M.; Flanagan, T.B., Absorption of hydrogen by palladium-nickel-rhodium ternary alloys, *Journal of Alloys and Compounds* **1995**, 217, 2.
36. Kibria F. A.k.m.; Kubota, T.; Kagawa, A.; Sakamoto, Y., Measurements of hydrogen solubility and electrical resistance of some palladium–rhodium alloys by a gas phase technique, *International Journal of Hydrogen Energy* **1999**, 24, 8.
37. Denton, A. R.; Ashcroft, N. W., Vegard's law, Phys. *Rev. A* **1991**, 43, 3161.
38. Metropolis, N.; Ulam, S., The monte carlo method, *Journal of the American Statistical Association* **1949**, 44 (247), 335-341.
39. Metropolis, N.; Rosenbluth, A.W.; Rosenbluth, M.N.; Teller, A.H.; Teller, E., Equations of State Calculations by Fast Computing Machines, *Journal of Chemical Physics* **1953,** 21 (6), 1087–1092
40. Sakamoto,Y.; Hirata, S. ; Nishikawa, H., Diffusivity and solubility of hydrogen in Pd-Ag and Pd-Au alloys, *Journal of the Less-Common Metals* **1982**, 88, 387 -395.
41. Okamoto, H.; Massalski, T., B., Binary Alloy Phase Diagrams 2nd ed., edited by T. B. Massalski, *ASM International*, Materials Park, Ohio, **1990**, 1, 409–410.
42. Wicke E.; Brodowsky, H., *Hydrogen in Metals 2* **1978**, 29, 73-151.
43. Katsusa H.; J. Farraro R.; McLellan R. B., The diffusivity of Hydrogen in palladium, *Acta Metallurgica* **1979**, 27, 1111-1114.
44. Holleck G. L., Diffusion and solubility of hydrogen in palladium and palladium--silver alloys, *J. Phys. Chem*. B **1970,** 74, 503.
45. Koffler S. A.; Hudson J. B.; Ansell G. S., Hydrogen Permeation through -Palladium, *Trans. Metall. Soc. AIME* **1969,** 245, 1735.
46. Toda G. J., Rate of permeation and diffusion coefficient of hydrogen through palladium, *Res. Inst. Catal*. **1958,** 6, 13-19.
47. Gryaznov V., Metal containing membranes for the production of ultrapure hydrogen and the recovery of hydrogen isotopes, *Sep. Purif. Methods* **2000**, 29, 171.
48. McKinley D. L., *US Patent Office 3,439,474* **1969** (Union Carbide).
49. Sakamoto, F.; Chen, F., L; Kinari, Y.; Sakamoto, Y., Hydrogen permeation through palladium alloy membranes in mixture gases of 10% nitrogen and ammonia in the hydrogen, *Int. J. Hydrogen Energy* **1997**, 22, 369.
50. Santos, D. S. d.; Azambuja, V. M., Pontonnier L.; Miraglia S.; Fruchart D.; *J. Alloys and Compounds* **2003,** 356-357, 236-239.